DOI: 10.19884/j.1672-5220.202404012

Mesoporous Carbon Nanofibers Loaded with Ordered PtFe Alloy Nanoparticles for Electrocatalytic Nitrate Reduction to Ammonia

XIE Meng, LUO Wei*, QIU Pengpeng*
State Key Laboratory for Modification of Chemical Fibers and Polymer Materials, College of Materials Science and Engineering, Donghua University, Shanghai 201620, China

Abstract: Highly dispersed bimetallic alloy nanoparticle electrocatalysts have been demonstrated to exhibit exceptional performance in driving the nitrate reduction reaction (NO_3RR) to generate ammonia (NH_3). In this study, we prepared mesoporous carbon nanofibers (mCNFs) functionalized with ordered PtFe alloys (O-PtFe-mCNFs) by a composite micelle interface-induced co-assembly method using poly(ethylene oxide)-block-polystyrene (PEO-*b*-PS) as a template. When employed as electrocatalysts, O-PtFe-mCNFs exhibited superior electrocatalytic performance for the NO_3RR compared to the mCNFs functionalized with disordered PtFe alloys (D-PtFe-mCNFs). Notably, the NH_3 production performance was particularly outstanding, with a maximum NH_3 yield of up to 959.6 μmol/(h·cm^2). Furthermore, the Faraday efficiency (FE) was even 88.0% at −0.4 V vs. reversible hydrogen electrode (RHE). This finding provides compelling evidence of the potential of ordered PtFe alloy catalysts for the electrocatalytic NO_3RR.

Key words: ordered PtFe alloy; mesoporous carbon nanofiber (mCNF); nitrate reduction reaction (NO_3RR); ammonia (NH_3) production reaction
CLC number: O611 **Document code**: A
Article ID: 1672-5220(2024)04-0365-12

Open Science Identity (OSID)

0 Introduction

Ammonia (NH_3) is not only a key ingredient in nitrogen fertilizers but also considered as a green and carbon-free hydrogen-rich fuel in industry[1-2]. However, although the conventional Haber-Bosch process allows for a reliable synthesis of industrial NH_3, it relies on high-temperature (300–550 ℃) and high-pressure (15–25 MPa) conditions, and leads to a significant depletion of the global energy supply[3-5]. As an alternative, electrocatalytic reduction of nitrate (NO_3^-) has received more attention due to the lower dissociation energy of the N═O bond and its widespread presence as an environmental pollutant[6-7]. However, the conversion of NO_3^- to NH_3 involves a complex 8-electron reaction process, which results in relatively slow reaction kinetics[8-10]. Alloying is a unique and commonly used approach that can modify the physicochemical properties of metal electrocatalysts and stabilize key intermediates of the multistep reaction, thereby improving the selectivity of nitrate reduction reaction (NO_3RR) electrocatalytic NH_3 synthesis[11-12]. Despite some promising advances in this field, the Faraday efficiency (FE) and NH_3 yields in the selective electrocatalytic process of NO_3^- to NH_3 are still lower than expected[13]. Intermetallic compounds are notable for their highly ordered atomic arrangements and well-defined d-orbital interactions[14-15]. These compounds possess unique geometrical and electronic properties that can significantly enhance catalytic activity and stability[16-17]. Furthermore, the orderliness of their atomic arrangements ensures a high degree of homogeneity of the active sites[18-19]. However, synthesizing ordered intermetallic alloys usually requires high-temperature annealing treatment, which often leads to particle aggregation, especially at high loadings[20-23]. To overcome this challenge, it is necessary to identify a suitable carrier that can effectively prevent particle aggregation. Mesoporous materials, in particular carbon nanofibers (CNFs) with high specific surface areas and open pores, are promising substrates due to their unique physical and chemical properties[24].

In light of these research advances, we sought to combine the advantages of ordered platinum-based alloys and mesoporous carbon carrier structures. To this end, ordered PtFe alloy functionalized mesoporous carbon nanofibers (mCNFs) were synthesized by employing poly(ethylene oxide)-block-polystyrene (PEO-*b*-PS) as a templating agent in conjunction with composite micellar

Received date: 2024-04-22
Foundation items: National Natural Science Foundation of China (Nos. 52225204, 52173233 and 52202085); Innovation Program of Shanghai Municipal Education Commission, China (No. 2021-01-07-00-03-E00109); Natural Science Foundation of Shanghai, China (No. 23ZR1479200); "Shuguang Program" Supported by Shanghai Education Development Foundation and Shanghai Municipal Education Commission, China (No. 20SG33); Fundamental Research Funds for the Central Universities, China (No. 2232024Y-01); DHU Distinguished Young Professor Program, China (Nos. LZA2022001 and LZB2023002)
* Correspondence should be addressed to QIU Pengpeng, email: qiupengpeng@dhu.edu.cn; LUO Wei, email: wluo@dhu.edu.cn
Citation: XIE M, LUO W, QIU P P. Mesoporous carbon nanofibers loaded with ordered PtFe alloy nanoparticles for electrocatalytic nitrate reduction to ammonia[J]. *Journal of Donghua University (English Edition)*, 2024, 41(4): 365-376.

interface-induced co-assembly. The resulting material, mCNFs functionalized with ordered PtFe alloys, designated O-PtFe-mCNFs, represented a notable advancement in the field of nanotechnology. The catalysts exhibited excellent performance in NH_3 production by nitrate reduction compared to the mCNFs functionalized with disordered PtFe alloys (D-PtFe-mCNFs), with a maximum NH_3 yield of 959.6 μmol/(h · cm^2) and an FE of 88.0% at −0.4 V vs. RHE. These results demonstrate the excellent electrochemical catalytic nitrate reduction NH_3 production performance of the catalysts.

1 Materials and Methods

1.1 Materials and reagents

Styrene, petroleum ether, tetrahydrofuran (THF), pyridine, cuprous bromide (CuBr), ammonium hydroxide (NH_4OH, with a mass fraction of 28% – 30%), dopamine (DA) hydrochloride, ferric (III) acetylacetonate, platinum (IV) chloride hexahydrate ($H_2PtCl_6 \cdot 6H_2O$) and ethanol were purchased from Shanghai Chemical Corp., China. 2-Bromoisobutyryl bromide and *N*, *N*, *N*', *N*', *N*'-pentamethyldiethylenetriamine (PMDETA) were purchased from Aladdin Industrial Co., Ltd., China. Poly (ethylene oxide) with a relative molecular mass of 5 000 (PEO-5000), potassium hydroxide (KOH) and commercial Pt/C (mass fraction of Pt is 20%) were purchased from Sigma-Aldrich, USA.

1.2 Synthesis of PEO-*b*-PS diblock copolymer

PEO-*b*-PS diblock copolymer was synthesized using an atom transfer radical polymerization (ATRP) method, which involved two steps. In the first step, the micro-initiator PEO-Br was prepared through an acyl bromide reaction. In the second step, the previously prepared PEO-Br (5.00 g), along with CuBr (0.15 g), PMDETA (0.50 g) and styrene (35 mL), were added to an ampoule bottle and subjected to three freeze-pump-thaw cycles to remove any residual gases. Subsequently, petroleum ether (200 mL) was added to the solution to induce the precipitation of the PEO-*b*-PS diblock copolymer. The copolymer was collected, washed with petroleum ether, and then dried under vacuum conditions at 40 ℃.

1.3 Synthesis of O-PtFe-mCNFs

In a typical synthesis, PEO-*b*-PS (50 mg) was dissolved in THF (8 mL) to obtain a transparent solution. After stirring for 5 min, DA hydrochloride (80 mg) was added. Sequentially adding metal salts (ferric (III) acetylacetonate, platinum (IV) chloride hexahydrate) and reacting for 5 min, the solution became purple-red and then black owing to metal ions' high oxidation capability. Then, CNFs (1 mg) were injected into the solution above. After reacting, the as-made samples were obtained by centrifuging and washed using water. The obtained black precipitates were freeze-dried and then carbonized at 750 ℃ in an NH_3 atmosphere.

1.4 Synthesis of D-PtFe-mCNFs

As a comparison, D-PtFe-mCNFs were prepared in an N_2 atmosphere.

1.5 Material characterizations

Ultraviolet (UV)-visible absorption spectra were acquired using a UV-1900i instrument (Shimadzu, Japan). The morphologies of catalysts were investigated using scanning electron microscopy (SEM) (TESCAN/MAIA3, Czech), transmission electron microscopy (TEM), and high angle angular dark field-scanning transmission electron microscopy (HAADF-STEM). Energy-dispersive X-ray spectroscopy (EDS) elemental mapping analysis was acquired using Talos F200S (Japan) operated at 200 kV. X-ray diffraction (XRD) measurement was conducted using a Rigaku D/Max-2550 PC diffractometer (Japan). Raman spectra were acquired using a reflex Invia-Reflex Raman microscope with a 532 nm laser excitation (Britain). X-ray photoelectron spectroscopy (XPS) spectra were obtained using an Escalab 250Xi (Japan) equipped with Al K radiation. N_2 sorption was carried out with Quantachrome Autosorb-iQ (German) to measure Brunauer-Emmett-Teller (BET) surface area and pore size distribution. Inductively coupled plasma (ICP) spectra were obtained using Prodigy-ICP (USA).

1.6 Electrochemical measurements

In a typical three-electrode cell system, platinum (1 cm^2) was the counter electrode at the position of the anode, and a saturated mercurous chloride electrode was used as a reference electrode to balance the potential. O-PtFe-mCNFs could be firsthand used as the cathode electrode. Electrochemical tests were conducted on a CHI 660D (Shanghai CHI Instruments Co., China). All potentials measured for saturated calomel electrodes (SCEs) were converted to a reversible hydrogen electrode (RHE) scale.

$$E_{RHE} = E_{SCE} + 0.2514 + 0.059\,H, \quad (1)$$

where E_{RHE} is the electrode potential against the RHE; E_{SCE} is the applied potential against the SCE; H is the pH value.

The electrochemical double-layer capacitance C_{dl} was calculated via linear fitting of the capacitive current densities at 0.35 V vs. RHE, as a function of the scan rate. The slope obtained from this fitting represented the value of C_{dl}. The electrochemical active surface area (ESCA) A_{ECSA} of the catalysts was subsequently calculated as

$$A_{ESCA} = \frac{C_{dl}}{C_s}, \quad (2)$$

where C_s is assumed to be 40 μF/cm^2, which is the general specific capacitance for an atomically smooth planar surface under homogeneous electrolytic conditions.

2 Results and Discussion

2.1 Morphological analyses of O-PtFe-mCNFs and D-PtFe-mCNFs

The PtFe alloy nanoparticles were confined in a one-dimensional mCNF framework by an interfacial mononuclear assembly strategy, followed by carbonization in an NH_3 atmosphere. Firstly, upon the addition of DA, metal ions and PEO-*b*-PS to a mixed water/ethanol solution, the phenolic hydroxyl group in DA complexed with the metal ions and formed DA-PtFe. As shown in Fig. 1, the UV-visible absorption spectrum of DA-PtFe ion solution reveals an additional peak at 440 nm induced by ligand-to-metal charge transfer, which confirms the formation of DA-PtFe ion complexes.

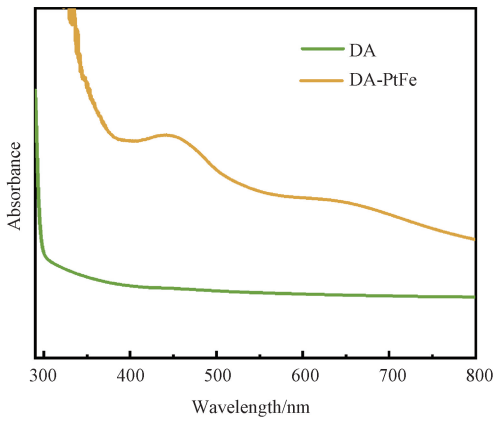

Fig. 1 UV-visible absorption spectra of DA and DA-PtFe ion solution

Subsequently, DA-PtFe ion complexes further interacted with the PEO segment of PEO-*b*-PS to form metal-organic composite cluster crystals. Firstly, upon the addition of acid-treated CNFs, the composite cluster crystals were attached to their surfaces due to electrostatic and hydrogen bonding interactions. Then, with the extension of reaction time, the adjustment of solution pH would trigger the cross-linking of DA. Finally, the metal-DA organic-inorganic composite structure was formed. Figure 2 shows the TEM images of the samples extracted at different reaction time. As the reaction time increases, the composite micelles are more uniformly attached to the surface of CNFs due to electrostatic and hydrogen bonding interactions.

The above superstructures were annealed in an NH_3 atmosphere at 750 ℃ to form O-PtFe-mCNFs. SEM images (Figs. 3(a) and 3(b)) and TEM images (Figs. 3(c) and 3(d)) demonstrate that the mCNFs exhibit a uniform mesoporous structure, with pore sizes distributed uniformly at approximately 10 nm. Among these, the PtFe alloy nanoparticles are dispersed uniformly throughout the entire framework, contributing to the enhancement of the catalyst activity through this homogeneous dispersion. The particles are protected by the CNF carrier which prevents agglomeration after high-temperature annealing and enables the catalysts to maintain stable catalytic performance. The EDS elemental mappings of the PtFe alloy nanoparticles (Figs. 3(e)–3(g)) reveal overlapping distributions of Fe and Pt elements, indicative of the formation of the PtFe alloy nanoparticles.

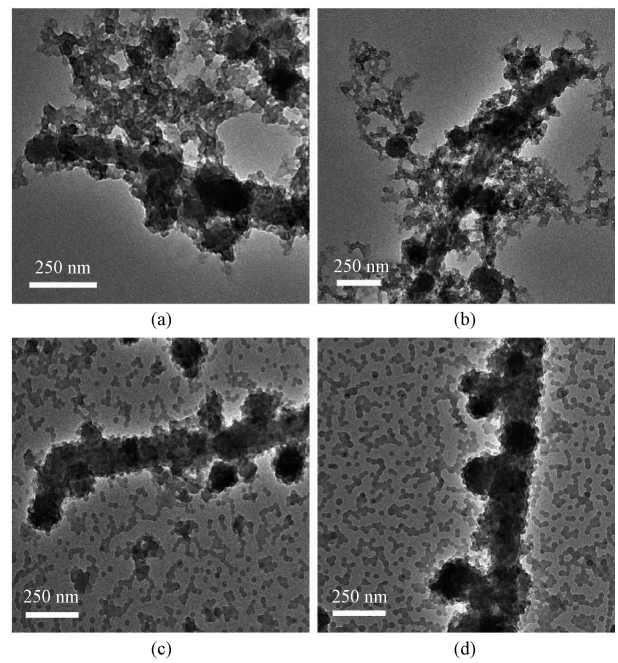

Fig. 2 TEM images of samples extracted at different reaction time: (a) 0 min; (b) 15 min; (c) 1 h; (d) 8 h

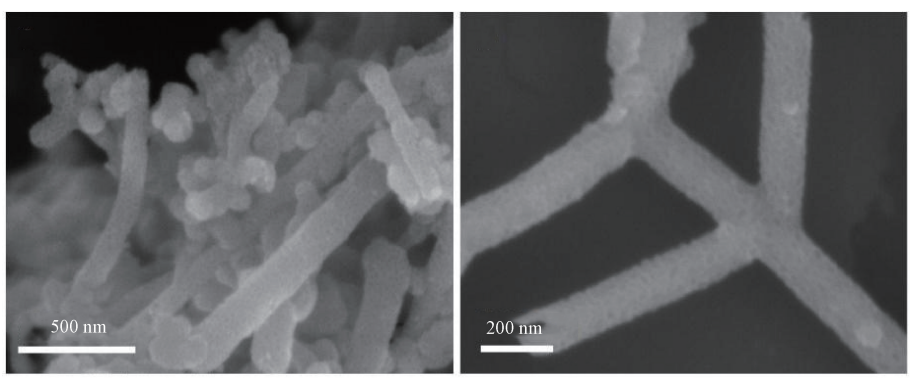

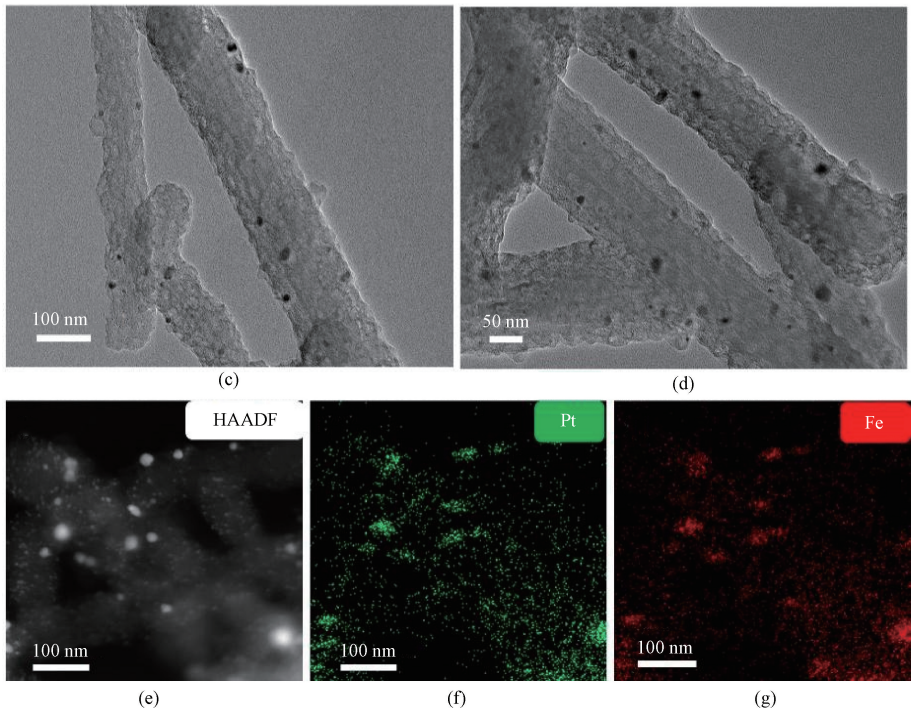

Fig. 3 Morphological analyses of O-PtFe-mCNFs: (a)–(b) SEM images; (c)–(d) TEM images; (e)–(g) HAADF-STEM image and corresponding EDS elemental mappings

D-PtFe-mCNFs were prepared under an N_2 atmosphere. Through detailed observation by SEM (Figs. 4(a) and 4(b)) and TEM (Figs. 4(c) and 4(d)), it is found that D-PtFe-mCNFs exhibit a core-shell structure similar to that of O-PtFe-mCNFs. Furthermore, the elemental distribution of D-PtFe-mCNFs was analyzed in detail using EDS elemental mapping. As demonstrated in Figs. 4(e)–4(g), the uniform distribution of metal elements confirms the formation of the PdFe alloy nanoparticles.

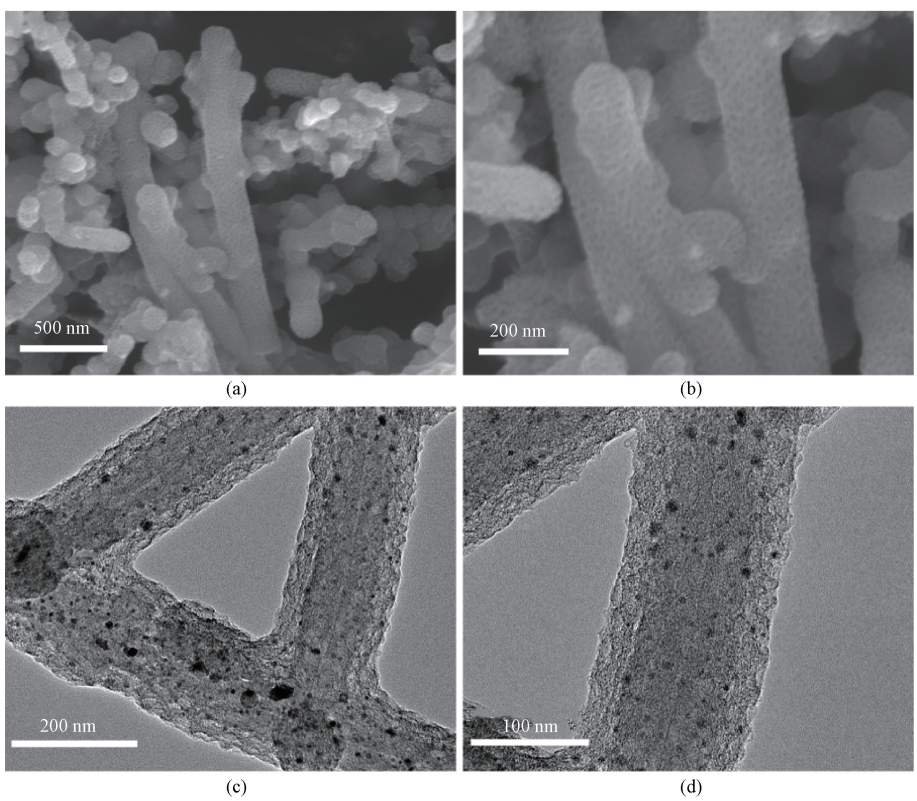

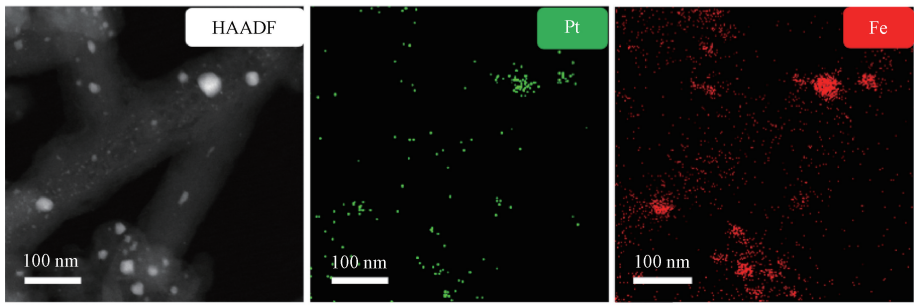

Fig. 4 Morphological analyses of D-PtFe-mCNFs: (a)–(b) SEM images; (c)–(d) TEM images; (e)–(g) HAADF-STEM image and corresponding EDS elemental mappings

2.2 Structural analyses of O-PtFe-mCNFs and D-PtFe-mCNFs

The crystal shape and the structure of Fe-mCNFs, Pt-mCNFs, O-PtFe-mCNFs and D-PtFe-mCNFs were analyzed by XRD. As can be seen from the XRD spectra (Fig. 5(a)), the broader diffraction peaks appear near 25° and correspond to the carbon carriers[25]. By the inquiry of power diffraction file (PDF), in contrast to the XRD spectra of Fe-mCNFs (PDF # 52-0513) and Pt-mCNFs (PDF#46-1043), the XRD diffraction peaks of O-PtFe-mCNFs exhibit significant clarity and the diffraction peak intensities are markedly elevated. This is attributed to the alloying of the two metals (Pt and Fe) under the influence of high temperature, and the strengthening of the electronic interactions between Pt and Fe results in a more regular and organized crystalline shape. O-PtFe-mCNFs exhibit discernible diffraction peaks of the Pt crystal structure at 2θ values of approximately 40.6° and 47.2°, corresponding to the (111) and (200) crystal faces of Pt, respectively. In addition, a detailed study reveals that the diffraction peak of O-PtFe-mCNFs at the 2θ position of the Pt (111) crystal face undergoes a significant positive shift compared to that of Pt-mCNFs. This directly suggests that the alloying of Pt with Fe has occurred. It is noteworthy that O-PtFe-mCNFs exhibit small and sharp diffraction peaks near 2θ of approximately 23.1° and 32.7°, which can be attributed to the (001) and (110) superlattice diffraction peaks of the intermetallic compound PtFe, respectively (PDF # 65-3253). The appearance of such superlattice diffraction peaks confirms the formation of the alloy with a chemically ordered structure. In contrast, as shown in Fig. 5(b), the XRD spectrum of D-PtFe-mCNFs exhibits the characteristics of a typical disordered PtFe alloy, with only two diffraction peaks at 42.3° and 49.3°, corresponding to (111) and (200), respectively (PDF#04-02-8944)[26]. It can be demonstrated that the interfacial single-beam assembly strategy, when combined with the NH_3 heat treatment process, results in the ordering of PtFe alloys.

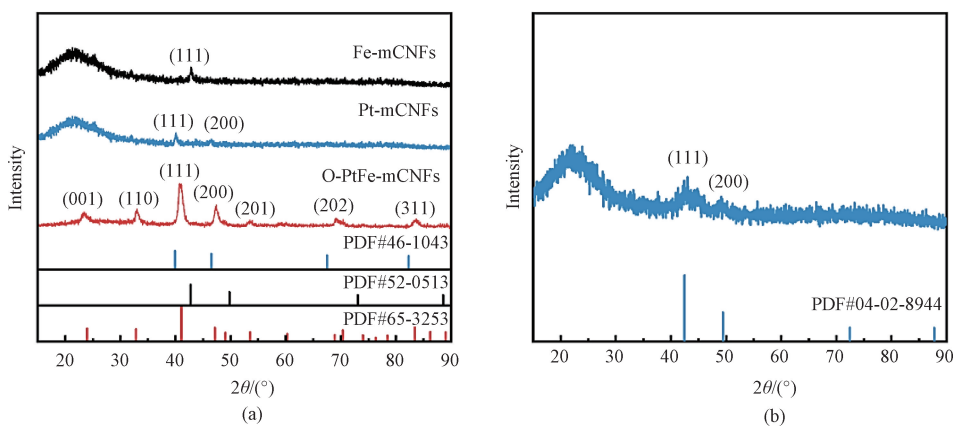

Fig. 5 XRD spectra of samples: (a) Fe-mCNFs, Pt-mCNFs and O-PtFe-mCNFs; (b) D-PtFe-mCNFs

XPS was employed to elucidate the electronic structures of O-PtFe-mCNFs and D-PtFe-mCNFs. The total spectra (Fig. 6(a)) unambiguously demonstrate the presence of the elements C, O, N, Fe and Pt. The high-resolution XPS spectra of all metal elements reveal that the intensity of the metallic state peaks in O-PtFe-mCNFs is higher than that in D-PtFe-mCNFs, indicating enhanced electronic interactions between the metal atoms in the more ordered distribution of O-PtFe-mCNFs. The N 1s spectra can be decomposed into pyridinic-N (398.2 eV), pyrrolic-N (399.6 eV) and graphitic-N (401.0 eV)[27]. The pyridinic-N and graphitic-N have a strong electron-donating ability, thus accelerating the electron transfer and the electrocatalytic reduction reaction. The contents

of pyridinic-N and graphitic-N in O-PtFe-mCNFs are significantly higher than those in D-PtFe-mCNFs (Fig. 6(b)). Figure 6(c) illustrates the split-peak spectrum of O-PtFe-mCNFs, Pt 4f. The peaks with binding energies at 72.1 eV and 75.4 eV correspond to the 0-valence state Pt(0)[28], which is shifted in a negative direction (0.23 eV) in O-PtFe-mCNFs as compared to the peak position of the Pt(0) binding energy in D-PtFe-mCNFs. Figure 6(d) shows the spectrum of Fe 2p in O-PtFe-mCNFs. The peak around 706.2 eV corresponds to pure Fe in the 0-valence state Fe(0)[29]. The binding energy peak position of Fe 2p in O-PtFe-mCNFs is shifted in the positive direction (0.37 eV) as compared to that of Fe(0) in D-PtFe-mCNFs. This shift can be attributed to the formation of an alloy between Pt and Fe. The presence of Fe in the Pt lattice results in the interaction of Pt with Fe, which in turn affects the electronic structure of Pt due to the difference in electronegativity. This change positively affects the adsorption capacity of the catalyst for nitrate.

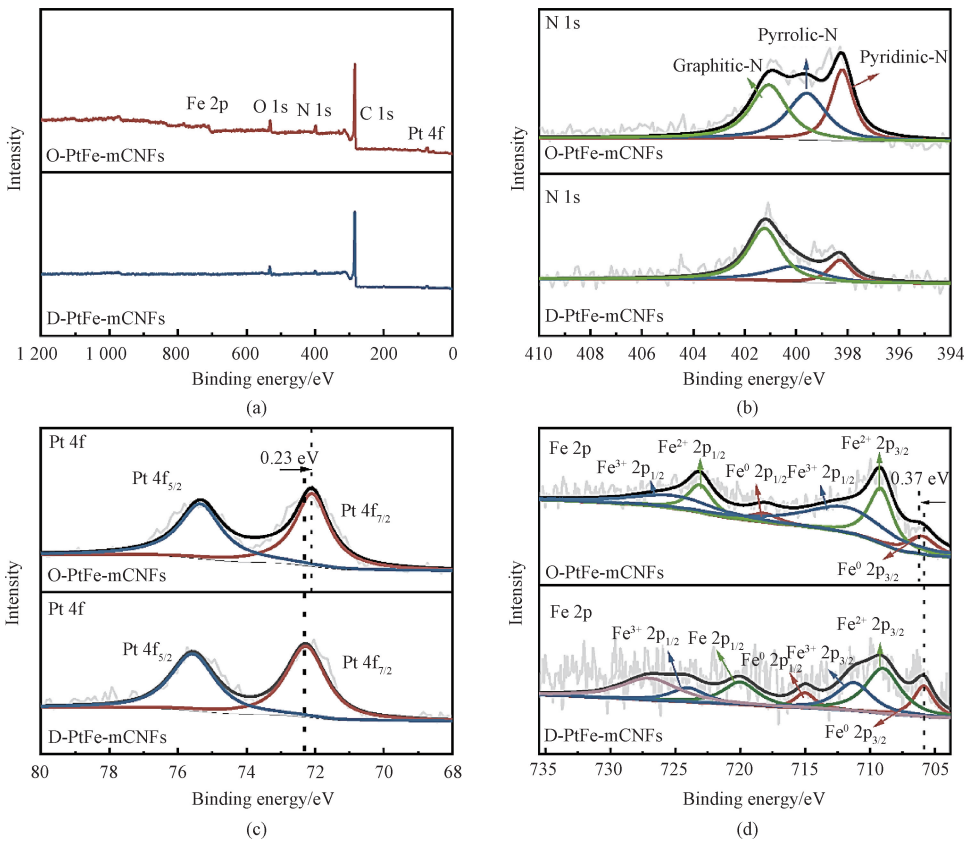

Fig. 6 XPS spectra of O-PtFe-mCNFs and D-PtFe-mCNFs: (a) total spectra; (b) N 1s; (c) Pt 4f; (d) Fe 2p

Nitrogen adsorption-desorption isotherms were employed to ascertain the BET specific surface area and the pore property of O-PtFe-mCNFs and D-PtFe-mCNFs, as shown in Figs. 7(a) and 7(b). In Fig. 7(b), dV/dD represents the change in pore volume V corresponding to a unit change in pore diameter D. In the range of a relative pressure of 0.4–0.8, the pore structure of both materials exhibit a typical IV-type curve with a distinct H_2 hysteresis loop, indicative of a mesoporous structure[30]. The BET specific surface areas of O-PtFe-mCNFs and D-PtFe-mCNFs are 282.62 m^2/g and 222.18 m^2/g, respectively, while their pore volumes are 0.43 cm^3/g and 0.34 cm^3/g, correspondingly. The BET specific surface area and pore volume of O-PtFe-mCNFs are larger than those of D-PtFe-mCNFs. This can be attributed to the NH_3 etching, which leads to the enhancement of micropores in the carbon frameworks and thus provides more surface for the catalytic reaction. The PtFe alloy mCNFs have adsorption branch pore size distributions all centered on 10 nm. These findings are in good agreement with the TEM observations. The BET results indicate that O-PtFe-mCNFs have larger surface area and more mesoporous pores. These characteristics can facilitate the reduction of nitrates by providing abundant active sites and exposing more active sites, which can also promote mass transfer and electron transfer effectively.

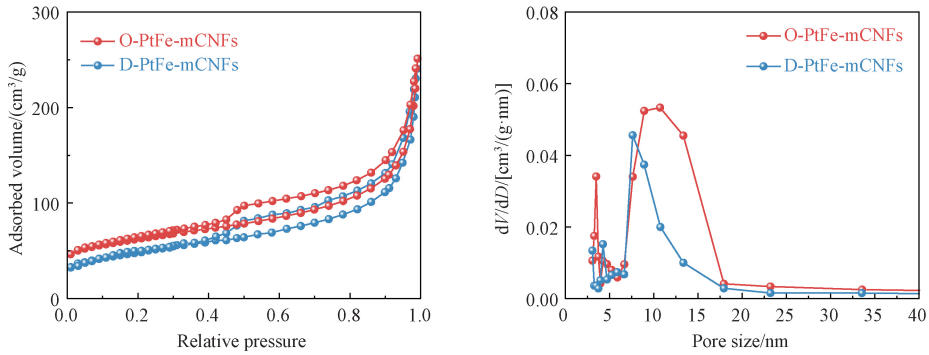

Fig. 7 BET specific surface area and pore property of O-PtFe-mCNFs and D-PtFe-mCNFs: (a) N_2 adsorption and desorption curves; (b) pore size distribution

As shown in Fig. 8, the Raman spectra of the resulting catalysts exhibit two peaks at 1 340 cm^{-1} (D band) and 1 588 cm^{-1} (G band)[31]. The former is indicative of sp^3 disordered carbon, while the latter is representative of sp^2 graphitic carbon. The intensity ratio of the D band to the G band I_D/I_G is indicative of the degree of graphitization and the defect density of the carbon-based materials. The I_D/I_G values of O-PtFe-mCNFs and D-PtFe-mCNFs are 0.83 and 0.63, respectively, suggesting that NH_3 annealing results in nitrogen enrichment within the carbon-based matrix, thereby increasing the number of defect sites.

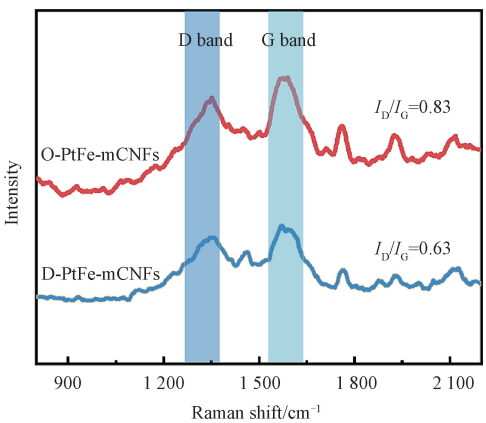

Fig. 8 Raman spectra of O-PtFe-mCNFs and D-PtFe-mCNFs

ICP analyses of O-PtFe-mCNFs and D-PtFe-mCNFs were performed. The ICP results shown in Table 1 demonstrate that the mass fractions of Fe and Pd are consistent with the metal additions.

Table 1 Elemental analysis results

Sample	Mass fraction of Fe/%	Mass fraction of Pd/%
O-PtFe-mCNFs	10.57	10.33
D-PtFe-mCNFs	12.24	10.46

2.3 Electrochemical NO_3RR performance

O-PtFe-mCNFs were initially evaluated in a standard three-electrode H-cell with a linear scanning voltammetric (LSV) curve. Figure 9(a) illustrates the outcomes of the measurements conducted on O-PtFe-mCNFs in a 1 mol/L KOH electrolyte without NO_3^- and with an NO_3^- mass concentration of 1 400 mg/L, respectively. The curve current density J growth in the electrolyte containing NO_3^- is significantly faster than that in the electrolyte without NO_3^-. This is mainly because the presence of NO_3^- promotes the increase in current density, thereby revealing the occurrence of the NO_3RR. Furthermore, in comparison to D-PtFe-mCNFs, O-PtFe-mCNFs exhibit a pronounced shift in potential, reaching −0.04 V vs. RHE. The onset potential is more positive, and the current density can reach 300 mA/cm^2 at −0.6 V vs. RHE (Fig. 9(b)). This suggests that O-PtFe-mCNFs exhibit enhanced activity in the electrocatalytic NO_3RR.

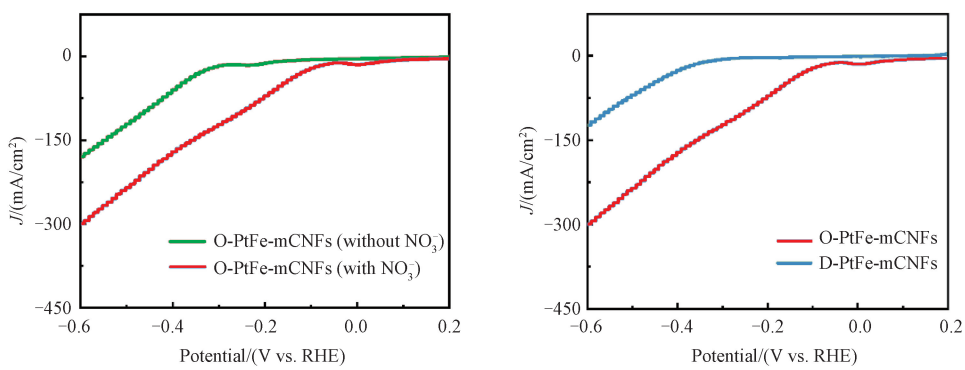

Fig. 9 LSV curves: (a) O-PtFe-mCNF with and without NO_3^- environment; (b) O-PtFe-mCNFs and D-PtFe-mCNFs with NO_3^- environment

To validate the results of LSV, FE and NH_3 yields at different voltages were measured and calculated. The calibration curves (A represents the absorbance; c is the concentration; R represents the correlation coefficient) of NO_3^-, NO_2^- and NH_4^+ as shown in Fig. 10 are first plotted using a colorimetric method to quantify the reactants and products. It can be seen from Fig. 11 that the NH_3 yields exhibit a pronounced increase when the potential is altered from −0.3 V vs. RHE to −0.7 V vs. RHE. Both O-PtFe-mCNFs and D-PtFe-mCNFs achieve the optimal NH_3 yields at a potential of −0.7 V vs. RHE. The NH_3 yields of O-PtFe-mCNFs and D-PtFe-mCNFs at −0.7 V vs. RHE are 959.6 μmol/(h · cm^2) and 578.63 μmol/(h · cm^2), respectively. Particularly at a potential of −0.4 V vs. RHE, O-PtFe-mCNFs for NH_3 synthesis reaches an FE of 88.0%, outperforming most of the reported catalysts (Table 2). O-PtFe-mCNFs possess stronger electrocatalytic nitrate reduction performance compared with D-PtFe-mCNFs. In addition, as shown in Fig. 12, the FE and NH_3 yields of O-PtFe-mCNFs decrease only slightly after 10 cycles, indicating their strong stability.

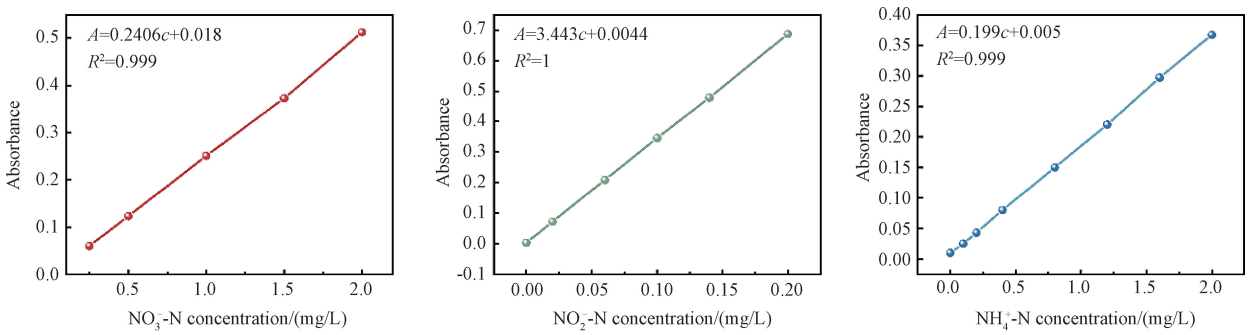

Fig. 10 Concentration-absorbance calibration curves: (a) NO_3^-; (b) NO_2^-; (c) NH_4^+

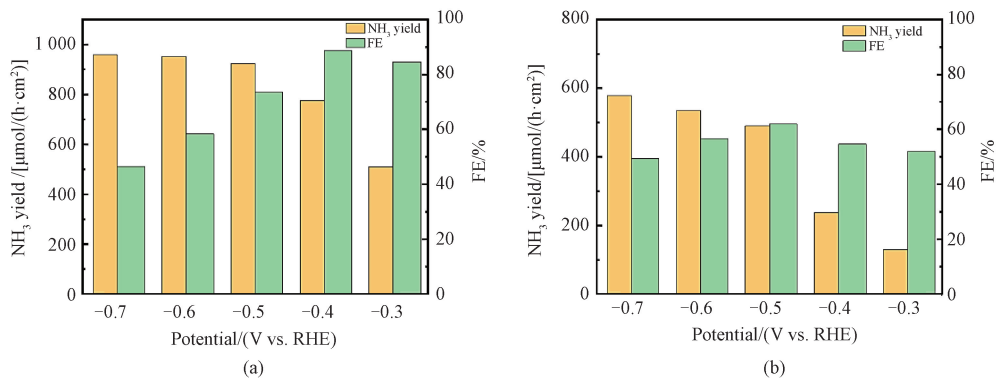

Fig. 11 NH_3 yield and FE plots: (a) O-PtFe-mCNFs; (b) D-PtFe-mCNFs

Table 2 Comparison of catalytic reaction performance of O-PdFe-mCNFs with catalysts reported in literature

Catalyst	Electrolyte	FE/%	NH_3 yield/ [μmol/(h·cm^2)]	Reference
O-PdFe-mCNFs	1.0 mol/L KOH+0.1 mol/L NO_3^-	88.0	959.6	This work
Fe SAC	0.1 mol/L K_2SO_4+0.5 mol/L NO_3^-	74.9	558.6	[21]
Pd NC	0.1 mol/L K_2SO_4+0.1 mol/L NO_3^-	79.9	666.0	[32]
Pd/TiO_2	1 mol/L LiCl+0.25 mol/L NO_3^-	92.0	65.8	[33]
Pd-Cu_2O	0.5 mol/L K_2SO_4+50×10^{-6} mol/L NO_3^-	96.5	54.4	[34]
Co-Fe@ Fe_2O_3	0.1 mol/L Na_2SO_4+50×10^{-6} mol/L NO_3^-	85.2	51.8	[35]
In-S-G	1.0 mol/L KOH+0.01 mol/L NO_3^-	75.0	74.8	[28]
NiFe@ Fe_3O_4	0.01 mol/L NaCl+0.003 mol/L NO_3^-	19.6	34.7	[36]
Ag-Ni films	1.0 mol/L NaOH+0.02 mol/L NO_3^-	83.0	100.0	[37]
CuNi NC	0.1 mol/L PBS+0.003 mol/L NO_3^-	79.6	12.9	[30]
Ru nanoclusters	1.0 mol/L KOH+1 mol/L NO_3^-	45.0	1 170.0	[38]

Notes: SAC is short for single-atom catalyst; NC is short for nanocrystalline; In-S-G is short for indium (In) in sulfur-doped graphene.

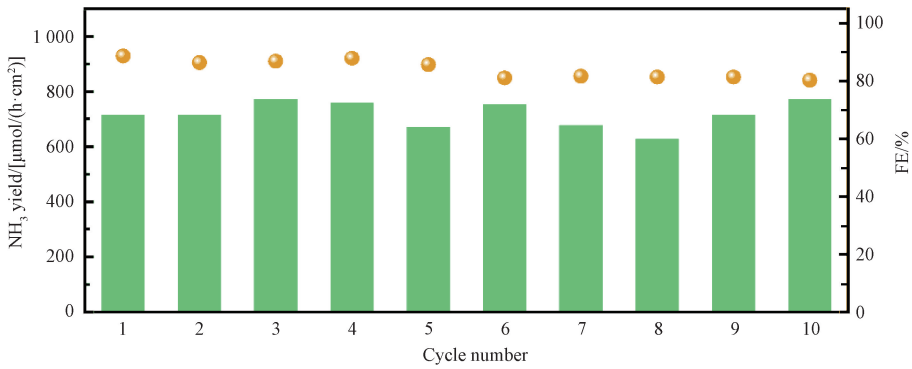

Fig. 12 NH_3 yield and FE of O-PtFe-mCNFs at −0.4 V vs. RHE after different cycle numbers

The C_{dl} values of O-PtFe-mCNFs and D-PtFe-mCNFs were tested. The cyclic voltammetry (CV) curves of D-PtFe-mCNFs exhibit a shuttle shape, while those of O-PtFe-mCNFs are more rectangular. The closed curve area of O-PtFe-mCNFs is significantly larger than that of D-PtFe-mCNFs, indicating that O-PtFe-mCNFs exhibit higher electrochemical activity (Fig. 13). Furthermore, the C_{dl} values are calculated, as shown in Fig. 14. The results demonstrate that the C_{dl} value of D-PtFe-mCNFs is 37.6 mF/cm^2, whereas the C_{dl} value of O-PtFe-mCNFs is as high as 49.7 mF/cm^2. This indicates that O-PtFe-mCNFs have a greater number of active sites. The calculation of ECSA is carried out using Eq. (2). Specifically, the ECSA of D-PtFe-mCNFs is 35.00 cm^2, while that of O-PtFe-mCNFs is as high as 86.50 cm^2. This remarkable advantage further confirms the high activity of O-PtFe-mCNFs in the electrocatalytic NO_3RR.

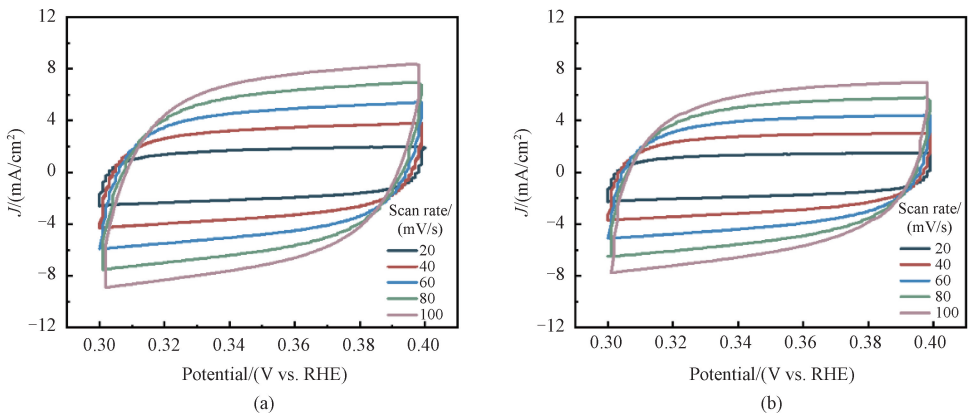

Fig. 13 CV curves with different scan rates: (a) O-PtFe-mCNFs; (b) D-PtFe-mCNFs

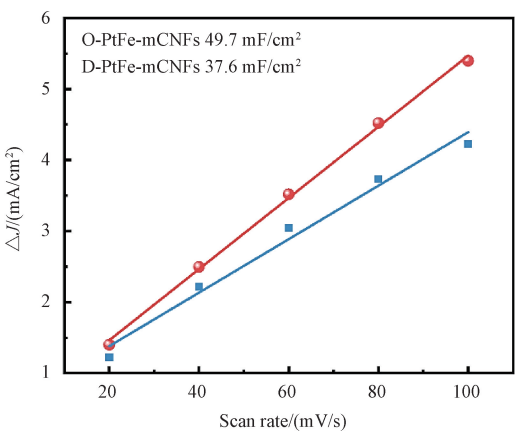

Fig. 14 C_{dl} curves of O-PtFe-mCNFs and D-PtFe-mCNFs

3 Conclusions

In this study, we synthesized O-PtFe-mCNFs using PEO-*b*-PS as a templating agent in combination with composite micellar interface-induced co-assembly. The resulting one-dimensional mCNFs exhibited a clear structure with a uniform mesopore size of approximately 10 nm. The ordered PtFe alloy nanoparticles were protected by the restricted domain of the mCNF carrier, and the particles did not agglomerate and grow after high-temperature annealing, which avoided the loss of activity. In comparison to D-PtFe-mCNFs, O-PtFe-mCNFs exhibited super-ordered lattice diffraction peaks (001) and (110). The interfacial single-beam assembly strategy, combined with the NH_3 heat treatment process could be employed to synthesize ordered PtFe alloys. The

high degree of alloying of Pt and Fe in the ordered PtFe alloys was demonstrated by the XPS analysis, which positively affected the adsorption capacity of the catalysts for nitrate. The electrocatalytic nitrate reduction performance of O-PtFe-mCNFs was evaluated, and the results demonstrated that O-PtFe-mCNFs exhibited superior activity in the electrocatalytic NO_3RR. O-PtFe-mCNFs exhibited excellent NH_3 production performance for nitrate reduction with a maximum NH_3 yield of 959.6 μmol/(h·cm^2), in comparison to D-PtFe-mCNFs. Furthermore, the FE of O-PtFe-mCNFs reached −0.4 V vs. RHE, with an efficiency of 88.0%. The ECSA increased by 2.5 times (86.50 cm^2), confirming the high activity of O-PtFe-mCNFs in the electrocatalytic NO_3RR. This further demonstrated the great potential of O-PtFe-mCNFs for the electrocatalytic NO_3RR.

References

[1] ZHANG Y Q, LIU H W, ZHAO S Y, et al. Insights into the dynamic evolution of defects in electrocatalysts[J]. *Advanced Materials*, 2023, 35(9): e2209680.

[2] LUO L H, WANG M L, CUI Y, et al. Surface iron species in palladium-iron intermetallic nanocrystals that promote and stabilize CO_2 methanation [J]. *Angewandte Chemie International Edition*, 2020, 59(34): 14434-14442.

[3] LI X, HE Y H, CHENG S B, et al. Atomic structure evolution of Pt-Co binary catalysts: single metal sites versus intermetallic nanocrystals [J]. *Advanced Materials*, 2021, 33(48): e2106371.

[4] PU Z H, LIU T T, ZHANG G X, et al. General synthesis of transition-metal-based carbon-group intermetallic catalysts for efficient electrocatalytic hydrogen evolution in wide pH range [J]. *Advanced Energy Materials*, 2022, 12(20): 2200293.

[5] GAO Q, PILLAI H S, HUANG Y, et al. Breaking adsorption-energy scaling limitations of electrocatalytic nitrate reduction on intermetallic CuPd nanocubes by machine-learned insights[J]. *Nature Communications*, 2022, 13: 2338.

[6] ZHANG R, HONG H, LIU X H, et al. Molecular engineering of a metal-organic polymer for enhanced electrochemical nitrate-to-ammonia conversion and zinc nitrate batteries [J]. *Angewandte Chemie International Edition*, 2023, 62(48): e202309930.

[7] ZHANG S, WU J H, ZHENG M T, et al. Fe/Cu diatomic catalysts for electrochemical nitrate reduction to ammonia [J]. *Nature Communications*, 2023, 14: 3634.

[8] WANG Y Z, ZHANG X Y, HE H J, et al. Ordered mesoporous high-entropy intermetallics for efficient oxygen reduction electrocatalysis [J]. *Advanced Energy Materials*, 2024, 14(8): 2303923.

[9] ZHOU Y Y, DUAN R Z, LI H, et al. Boosting electrocatalytic nitrate reduction to ammonia via promoting water dissociation[J]. *ACS Catalysis*, 2023, 13(16): 10846-10854.

[10] BUSCHOW K H J, VAN ENGEN P G, JONGEBREUR R. Magneto-optical properties of metallic ferromagnetic materials[J]. *Journal of Magnetism and Magnetic Materials*, 1983, 38(1): 0304885383900975.

[11] ASHIDA Y, ARASHIBA K, NAKAJIMA K, et al. Molybdenum-catalysed ammonia production with samarium diiodide and alcohols or water[J]. *Nature*, 2019, 568: 536-540.

[12] QI C H, YANG H Y, SUN Z Q, et al. Modulating electronic structures of iron clusters through orbital rehybridization by adjacent single copper sites for efficient oxygen reduction[J]. *Angewandte Chemie International Edition*, 2023, 62(39): e202308344.

[13] GAO W S, XIE K F, XIE J, et al. Alloying of Cu with Ru enabling the relay catalysis for reduction of nitrate to ammonia[J]. *Advanced Materials*, 2023, 35(19): e2202952.

[14] YANG C L, WANG L N, YIN P, et al. Sulfur-anchoring synthesis of platinum intermetallic nanoparticle catalysts for fuel cells[J]. *Science*, 2021, 374(6566): 459-464.

[15] LUO Y, ZHANG B P, LIU C C, et al. Sulfone-modified covalent organic frameworks enabling efficient photocatalytic hydrogen peroxide generation via one-step two-electron O_2 reduction [J]. *Angewandte Chemie International Edition*, 2023, 62(26): e202305355.

[16] ZHU G H, JIANG Y, YANG H Y, et al. Constructing structurally ordered high-entropy alloy nanoparticles on nitrogen-rich mesoporous carbon nanosheets for high-performance oxygen reduction[J]. *Advanced Materials*, 2022, 34(15): e2110128.

[17] CHEN W, LUO S P, SUN M Z, et al. Hexagonal PtBi intermetallic inlaid with sub-monolayer Pb oxyhydroxide boosts methanol oxidation[J]. *Small*, 2022, 18(14): e2107803.

[18] HE Y T, YANG X X, LI Y S, et al. Atomically dispersed Fe-Co dual metal sites as bifunctional oxygen electrocatalysts for rechargeable and flexible Zn-air batteries [J]. *ACS Catalysis*, 2022, 12(2): 1216-1227.

[19] WANG W J, MENG Y, ZHANG Y X, et al. Electrically switchable polarization in Bi_2O_2Se ferroelectric semiconductors [J]. *Advanced Materials*, 2023, 35(12): e2210854.

[20] ZHANG H, WANG C Q, LUO H X, et al. Iron nanoparticles protected by chainmail-structured graphene for durable electrocatalytic nitrate reduction to nitrogen[J]. *Angewandte Chemie International Edition*, 2023, 62(5): e202217071.
[21] WU Z Y, KARAMAD M, YONG X, et al. Electrochemical ammonia synthesis via nitrate reduction on Fe single atom catalyst[J]. *Nature Communications*, 2021, 12: 2870.
[22] TIAN J J, XUE Q F, YAO Q, et al. Inorganic halide perovskite solar cells: progress and challenges[J]. *Advanced Energy Materials*, 2020, 10(23): 2000183.
[23] ZHANG Y, ZHAO Q, DANIL B, et al. Oxygen-vacancy-induced formation of Pt-based intermetallics on MXene with strong metal-support interactions for efficient oxygen reduction reaction[J]. *Advanced Materials*, 2024: 2400198.
[24] ZHU X H, LIU M M, BU F X, et al. Ordered mesoporous nanofibers mimicking vascular bundles for lithium metal batteries[J]. *National Science Review*, 2024, 11(5): nwae081.
[25] ZHAO X Y, JIANG Y Z, WANG M F, et al. Optimizing intermediate adsorption via heteroatom ensemble effect over RuFe bimetallic alloy for enhanced nitrate electroreduction to ammonia[J]. *Advanced Energy Materials*, 2023, 13(31): 2301409.
[26] WANG Y T, ZHOU W, JIA R R, et al. Unveiling the activity origin of a copper-based electrocatalyst for selective nitrate reduction to ammonia[J]. *Angewandte Chemie International Edition*, 2020, 59(13): 5350-5354.
[27] YANG X Y, DENG Y, YANG H T, et al. Functionalization of mesoporous semiconductor metal oxides for gas sensing: recent advances and emerging challenges[J]. *Advanced Science*, 2022, 10(1): e2204810.
[28] WANG H M, HUANG J J, CAI J M, et al. In situ/operando methods for understanding electrocatalytic nitrate reduction reaction[J]. *Small Methods*, 2023, 7(7): e2300169.
[29] DENG Z Q, LIANG J, LIU Q, et al. High-efficiency ammonia electrosynthesis on self-supported Co_2AlO_4 nanoarray in neutral media by selective reduction of nitrate[J]. *Chemical Engineering Journal*, 2022, 435: 135104.
[30] DU F, LI J S, WANG C H, et al. Active sites-rich layered double hydroxide for nitrate-to-ammonia production with high selectivity and stability[J]. *Chemical Engineering Journal*, 2022, 434: 134641.
[31] HU T, WANG C H, WANG M T, et al. Theoretical insights into superior nitrate reduction to ammonia performance of copper catalysts[J]. *ACS Catalysis*, 2021, 11(23): 14417-14427.
[32] HAN Y, ZHANG X Y, CAI W W, et al. Facet-controlled palladium nanocrystalline for enhanced nitrate reduction towards ammonia[J]. *Journal of Colloid and Interface Science*, 2021, 600: 620-628.
[33] GUO Y, ZHANG R, ZHANG S C, et al. Pd doping-weakened intermediate adsorption to promote electrocatalytic nitrate reduction on TiO_2 nanoarrays for ammonia production and energy supply with zinc-nitrate batteries[J]. *Energy & Environmental Science*, 2021, 14(7): 3938-3944.
[34] XU Y, REN K L, REN T L, et al. Ultralow-content Pd in-situ incorporation mediated hierarchical defects in corner-etched Cu_2O octahedra for enhanced electrocatalytic nitrate reduction to ammonia[J]. *Applied Catalysis B: Environmental*, 2022, 306: 121094.
[35] REZAII N, MAHOWALD K, RYSKIN R, et al. A syntax-lexicon trade-off in language production[J]. *Proceedings of the National Academy of Sciences*, 2022, 119(25): e2120203119.
[36] JONOUSH Z A, REZAEE A, GHAFFARINEJAD A. Electrocatalytic nitrate reduction using Fe^0/Fe_3O_4 nanoparticles immobilized on nickel foam: selectivity and energy consumption studies[J]. *Journal of Cleaner Production*, 2020, 242: 118569.
[37] MATTAROZZI L, CATTARIN S, COMISSO N, et al. Electrodeposition of compact Ag-Ni films from concentrated chloride baths and their test in the reduction of nitrate in alkali[J]. *Electrochimica Acta*, 2020, 346: 136240.
[38] XING CY, XUE Y R, ZHENG X C, et al. Highly selective electrocatalytic olefin hydrogenation in aqueous solution[J]. *Angewandte Chemie International Edition*, 2023, 62(41): e202310722.

介孔碳纳米纤维负载有序 PtFe 合金纳米颗粒用于电催化硝酸盐还原产氨

谢　梦，罗　维*，邱鹏鹏*
东华大学 材料科学与工程学院，纤维材料改性国家重点实验室，上海 201620

摘　要：高分散的双金属合金纳米颗粒电催化剂通常在推动硝酸根还原反应产氨中表现出非凡的性能。该研究利用聚乙二醇−聚苯乙烯嵌段共聚物（PEO-*b*-PS）作为模板，通过复合胶束界面诱导共组装法，制备有序 PtFe 合金功能化的介孔碳纳米纤维复合材料。当用作电催化剂时，有序 PtFe 合金比无序 PtFe 合金对硝酸根还原反应表现出更优异的电催化性能。有序 PtFe 合金催化产氨性能尤为出色，最大氨产量达 959.6 μmol/(h · cm^2)。在电位相对于可逆氢电极为−0.4 V（−0.4 V vs. RHE）的条件下，其法拉第效率达 88.0%。这一发现充分展示了有序 PtFe 合金催化剂在电催化硝酸根还原反应方面的潜力。

关键词：有序 PtFe 合金；介孔碳纳米纤维；硝酸根还原；产氨反应